Research Square

Preprints are preliminary reports that have not undergone peer review.
They should not be considered conclusive, used to inform clinical practice,
or referenced by the media as validated information.

Influence of welding sequences on the accumulation evolution of angular distortion in thick-plate T-joint GMAW: Numerical simulation and modeling perspectives

Zhuohua Yu
Nanchang Jiaotong Institute
Xiaomin Liu
Nanchang Jiaotong Institute
Junpei Deng
Nanchang University - Qianhu Campus: Nanchang University
Yimeng Xie
Nanchang Jiaotong Institute
Yaqi Sun
Nanchang Jiaotong Institute
Yang Liu
Nanchang Jiaotong Institute
Jinghua Chen
Nanchang Jiaotong Institute
Yinshui He
heyingshui117@163.com

Nanchang University https://orcid.org/0000-0002-2039-0662

Research Article

Keywords: Thick plate T-joint, Welding sequence, K-groove, Angular distortion, Numerical simulation

Posted Date: October 6th, 2026

DOI: https://doi.org/10.21203/rs.3.rs-10977815/v1

License: This work is licensed under a Creative Commons Attribution 4.0 International License.
Read Full License

Influence of welding sequences on the accumulation evolution of angular distortion in thick-plate T-joint GMAW: Numerical simulation and modeling perspectives

Zhuohua Yu[a], Xiaomin Liu[a], Junpei Deng[b], Yimeng Xie[a], Yaqi Sun[a], Yang Liu[a], Jinghua Chen[a], Yinshui He[b,*]

a Nanchang Jiaotong Institute, Nanchang, 330100, China

b School of Resources & Environment, Nanchang University, Nanchang, 330031, China

*The corresponding authors are Yinshui He (heyingshui117@163.com).

Abstract: Web angular distortion (WAD) in thick-plate T-joints is highly dependent on welding sequences in gas metal arc welding (GMAW). A major challenge in controlling WAD stems from its unclear evolution characteristics, making it difficult to determine optimal weld planning strategies among various welding sequence combinations. This study examines the influence of pass-by-pass and layer-by-layer welding sequences on the cumulative evolution of WAD through numerical simulations and statistical regression modeling, focusing on 40 mm-thick high-strength low-alloy steel T-joints with a K-groove. To validate the proposed sequentially coupled thermal-elastic-plastic finite element model, welding tests are conducted using three welding sequences, with simulation results showing excellent agreement (maximum WAD deviation: 0.21°). Six expanded welding sequences are analyzed to further explore cumulative evolution characteristics of WAD. We find that 1) there are at least two significant evolution stages of WAD: an intense adjustment phase (40% of weld passes) followed by a gradual convergence phase (48% of passes), which is approached by a Sine-Exponential model; 2) the ratio of the average correction amount of WAD per weld pass respectively belonging to the two phases is remarkably consistent, approximately 69:5; 3) the correction capacities of each pass and layer can be described with the exponential function and quintic equation, corresponding to the pass-by-pass and layer-by-layer welding sequences, respectively; and 4) the diagonally-intersecting welding sequence proves more effective in controlling WAD. These findings contribute to developing optimal weld planning strategies for WAD control, enhancing manufacturing efficiency of thick plate T-joints.

Keywords: Thick plate T-joint, Welding sequence, K-groove, Angular distortion, Numerical simulation

1. Introduction

High-strength low-alloy steel is widely used in the manufacturing of large equipment due to its excellent mechanical properties and processability [1, 2]. T-joint components, as critical load-bearing elements, play a vital role in maintaining structural integrity and performance. They are fabricated in port machinery, pressure vessel manufacturing, building, etc. However, thick-plate T-joints with K-grooves (**Fig. 1**) are highly susceptible to web angular distortion (WAD) in gas metal arc welding (GMAW), particularly after multiple localized heating and rapid cooling cycles [3, 4]. Excessive WAD not only compromises the load-bearing capacity and assembly fit-up of components, but also leads to increased production cycles and higher manufacturing costs [5-7].

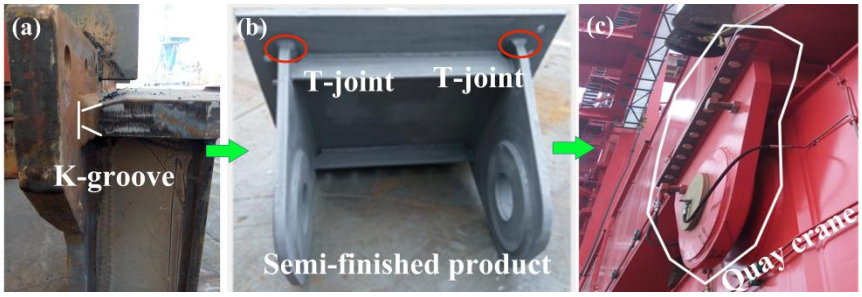


Fig. 1 Example of thick plate T-joints in the mechanical equipment. (a) A type of bearing. (b) Semi-finished product of the bearing. (c) Bearing in service.

WAD is influenced by a multitude of factors, including joint geometry [8], heat input parameters [9], welding restraints [10, 11], welding sequences [12-15] etc. They generally interact in complex ways. Even when only considering welding sequences, WAD in thick-plate T-joints remains a highly intricate and cumulative process, due to the vast number of possible combinations [16]. A key challenge lies in revealing the evolution characteristics of WAD in terms of welding sequences, to establish predictive models [17] or develop effective WAD control strategies [18, 19].

Numerous studies have revealed that the welding sequence has a significant impact on joint deformation. And these studies usually adopt finite element (FE) methods to reduce costs. A thermal-elastic-plastic FE model for naval EH36 steel T-joints reveals that the welding sequence critically affects distortion, and alternating welding paths between reinforcements significantly reduces distortion [20]. In [19], FE simulations of 9 mm-thick T-joints indicated that proper sequence and direction can reduce distortion by up to 40%. In addition, FE analyses of 6 mm and 9 mm T-joints in [21] revealed that the welding sequence markedly impacts angular distortion and longitudinal stress distribution, particularly in lower welding layers. Studies on other materials of thin-plate T-joints also confirm that welding sequences strongly influence welding distortion, such as Al6061-T6 aluminum alloy [22, 23] and 304 stainless steel [24-26].

To determine optimal welding sequences, numerous researchers have conducted related studies, primarily employing FE methods based on thermal-elastic-plastic models. Shao et al. [27] investigated four welding sequences on angular distortion in Q345D thin-plate T-joints using ANSYS. They concluded that the optimal sequence can effectively control residual stress and deformation. Rong et al. [28] studied six welding sequences considering welding directions on 316L austenitic stainless steel T-joints via ABAQUS. Ghafouri et al. [12] compared two sequences on welding-induced stresses and distortion in 6 mm-thick high-strength low-alloy T-joints through both FE simulation (ABAQUS) and experiments. Their subsequent study [29] on the same joint revealed the influence of welding sequences on WAD and residual stress magnitude.

The above studies on thin-plate T-joints involve a limited number of passes (two sides), which restricts the possible welding sequences, even when welding directions are considered. In those studies, a given welding path is divided into two or more sections to create multiple sequence combinations. In contrast, for thick-plate T-joint GMAW, later weld beads are deposited onto previously completed welds, which results in a pronounced superposition effect and leads to redistribution of thermal cycles and stresses. The multipass welding process alters the microstructure of the heat-affected zone. It also introduces complex transient thermal stresses and residual stress fields. Consequently, the evolution process of WAD in thick plate T-joints is more

complex, with welding sequence variations showing a greater influence on distortion outcomes than other process parameters [29].

Compared to the extensive research on thin-plate T-joint welding, studies on the influence of welding sequences on the WAD of thick-plate T-joints (typically with a thickness exceeding 20 mm) remain relatively limited. Zhang et al. [30] evaluated three welding sequences aimed at minimizing WAD in a 30 mm-thick T-joint with a single V-groove and over 14 passes using ABAQUS. Their results indicate that applying welding passes to the flange side results in the lowest WAD. In a subsequent study, the same research team achieved a 73% reduction in WAD by combining structural restraint with an optimized welding sequence [11]. Lan et al. [31] compared three welding sequences for a 15 mm-thick Q690 steel T-joint, noting that completing all welds on one side prior to the other led to the largest leftward tilting deformation, whereas alternating between sides resulted in smaller deformations. Manurung et al. [32] investigated a combined joint geometry consisting of two T-joints and one butt joint using finite element simulations and experiments, identifying an outside-to-inside welding sequence as optimal. Similarly, Li et al. [33] designed localized alternating sequences for 26 mm-thick T-joints with J-groove and K-groove configurations, observing that WAD accumulates incrementally with each weld layer. Despite these advances, two key research gaps remain regarding the evolution of WAD in thick-plate T-joints. First, the influence of welding sequences remains underexplored, particularly for web thicknesses exceeding 30 mm, where more than six sequence variations may be possible. Second, the progression of WAD across different welding stages has yet to be fully elucidated.

When welding thick plates, inadequate arc heat penetration at the weld root often occurs with direct welding. Grooving is therefore essential to ensure weld quality, with groove configurations significantly influencing the performance of thick-plate T-joints. Sharma and Shahi [34] evaluated 15-mm-thick welded joints with different groove designs, finding that K-groove configurations achieved higher yield strength and ultimate tensile strength. He et al. [35] compared WAD in K-groove and non-groove T-joints (8–12 mm thick), demonstrating that K-grooves substantially reduce distortion. Wei and Jiang [36] further supported this through finite element analysis of 12-mm-thick T-joints, showing K-grooves reduced residual stress peak regions by 27% compared to non-groove designs. Similarly, Zhang and Tian [24] concluded that double V-groove butt joints effectively mitigated angular and longitudinal distortion in multi-pass welds. K-grooves are widely recognized as an efficient design for thick plates. They enhance both weld quality and productivity. However, they require welding on both sides of the web. This necessity complicates the planning of weld sequences. In addition, the existing studies have not yet systematically investigated the evolution characteristics of the WAD in K-groove T-joints under different welding sequences.

Compared to heat input parameters, the welding sequence is a more macroscopic and adjustable influencing factor. Therefore, this study focuses on its impact on WAD in thick-plate T-joints. Since Q345D is a common high-strength steel mainly used in the manufacturing fields of pressure vessels, port machinery, and bridges, it is used as the welding base metal in this paper. The effects of welding sequences on WAD and residual stresses are fully investigated through FE simulation and statistical regression modeling, using K-groove T-joints. To streamline the study, welding direction is not considered in the sequence design, and a unilateral welding approach is adopted in both experiments and simulations.

Three 40 mm-thick T-joints are first welded under three typical welding sequences, and their

WAD results are analyzed to determine the settings for the simulation process. Based on the experimental data, a FE model is then developed in ABAQUS, and thermo-mechanical analysis is performed to simulate the three sequences, with results validated against welding results. Subsequently, six expanded welding sequences are examined using the FE model to analyze the cumulative evolution process of WAD. Statistical regression modeling eventually reveals the evolution characteristics of WAD across different welding stages, providing insights for optimizing welding sequences and enabling potential real-time angular distortion control in such joints.

The remainder of the paper is organized as follows. Section 2 presents the experimental procedure, including a graphical abstract. Section 3 gives the numerical analysis process in detail. In Section 4, the experimental results and discussion that mainly involve numerical simulation and data analysis results are described. Section 5 concludes the paper with a summary and prospect of future work.

2. Experimental procedure

In this study, the FE method is primarily employed to investigate the evolution characteristics of WAD. However, prior to conducting extensive numerical simulations, welding experiments and finite element modeling analyses were performed concurrently to assure the accuracy of the simulation results.

Three K-groove T-joints were fabricated using Q345D steel for accuracy assurance. The welding filler material is ER50-6 wire with a diameter of 1.2 mm, and the chemical compositions of the base material and the deposited metal are provided in **Table 1**. GMAW is employed with the shielding gas mixture of 80% Ar and 20% CO_2.

Table 1

Chemical compositions of Q345D steel and ER50-6 filler metal (wt. %).

Material	C	Si	Mn	P	S	Cr	Ni	Mo	Fe
Q345	0.16	0.33	1.42	0.017	0.013	0.07	0.08	0.08	Bal.
ER50-6	0.11	0.92	1.72	0.018	0.019	0.11	0.09	0.07	Bal.

Before welding, the web and flange plates were positioned perpendicularly using a fixture, maintaining a 4 mm root gap. The joints were secured by tack welding, followed by one-sided backing welding to ensure full root penetration. All three T-joints had the same dimensions: a 45° groove angle, 40 mm thick flange and web plates, and a longitudinal dimension of 200 mm (**Fig. 2**).

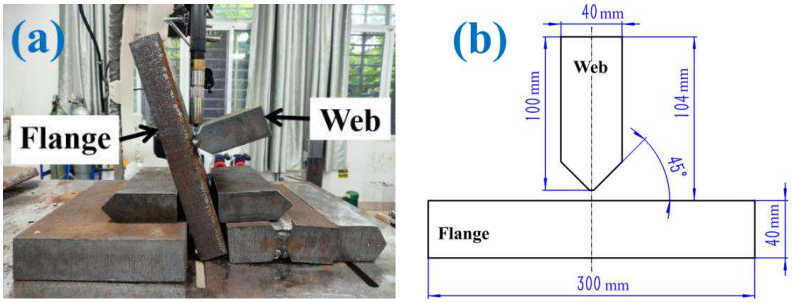


Fig. 2 Welded specimen of the T-joint. (a) T-joint in the welding state. (b) Joint geometry.

The three K-groove T-joints use different weld arrangements (**Fig. 3**) in GMAW, each consisting of 25 weld beads. In **Fig. 3** the numbers indicate the order of the weld bead. These sequences are based on practical experience.

- Case A uses an alternating side-by-side welding sequence. After depositing each bead, the welding location switches to the opposite side at the corresponding position until the groove is fully filled.
- Case B follows an alternating layer-by-layer sequence. Here, all weld beads for a given layer are completed on one side before moving to the opposite side for the same layer, repeating until the groove is filled.
- Case C adopts a one-side-first approach, where one entire side of the groove is welded before proceeding to the other side.

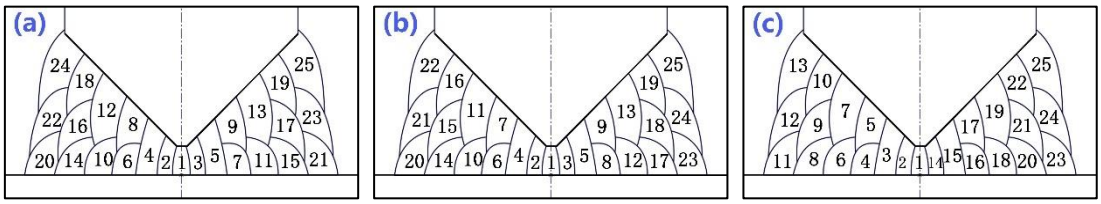


Fig. 3 Three sequences in welding tests for validation of the proposed FE method here. (a) Case A: Pass-by-pass alternating welding sequence. (b) Case B: Layer-by-layer alternating welding sequence. (c) Case C: Fully-welded one-sided sequence.

The same set of welding process parameters (**Table 2**) is used for welding tests of the three joints. They are determined by many welding tests and prior knowledge. All three welding tests are conducted with only one robot, using horizontal rolled position (for fillet welds). The weld is aligned within the weld zone by adjusting the welding torch angle, relative to the joint and workbench. Throughout the welding process, the T-joint remains unconstrained by external mechanical boundary conditions, and the interlayer temperature is maintained at approximately 100 °C.

Table 2

Welding process parameters used in welding tests.

Weld pass	Welding current (A)	Welding voltage (V)	Welding speed (mm/s)
1	180	22	5
2-3	200	23	5
4-5	230	26	5
6-11	220	25	5
12-13,16-19	235	27	5
14-15,20-25	220	24	5

Upon completion of each weld pass, the angle between the flange and web of the T-joint is measured using a triple-magnetic-face digital inclinometer (measurement accuracy: 0.01°). In measurement (**Fig. 4**), the upper surface of the flange serves as the 0° reference, and the angular deviation of the web relative to the flange is quantified against this baseline. Five measurement locations are marked at equal intervals along the welding direction, as illustrated in **Fig. 4b**.

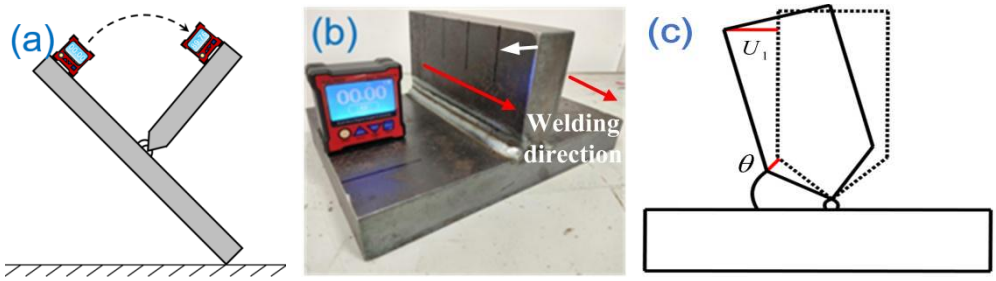


Fig. 4 Measurement method of WAD. (a) Schematic diagram of WAD measurement. (b) WAD measurement positions (the white arrow) and the welding direction. (c) The definitions of U_1 and θ.

In this study, the transverse displacement variation U_1 at the edge of the web is adopted as the evaluation metric for WAD. U_1 is calculated as

$$U_1 = 20(\cos\theta - 1) + 100\sin\theta \tag{1}$$

where θ represents the deflection angle (**Fig. 4c**).

After the measurement is completed, the test samples are cut at the middle of the joint, covering the weld and the heat affected zone. The weld quality is tested according to the related standard. The main research contents in the next sections are given in **Fig. 5**.

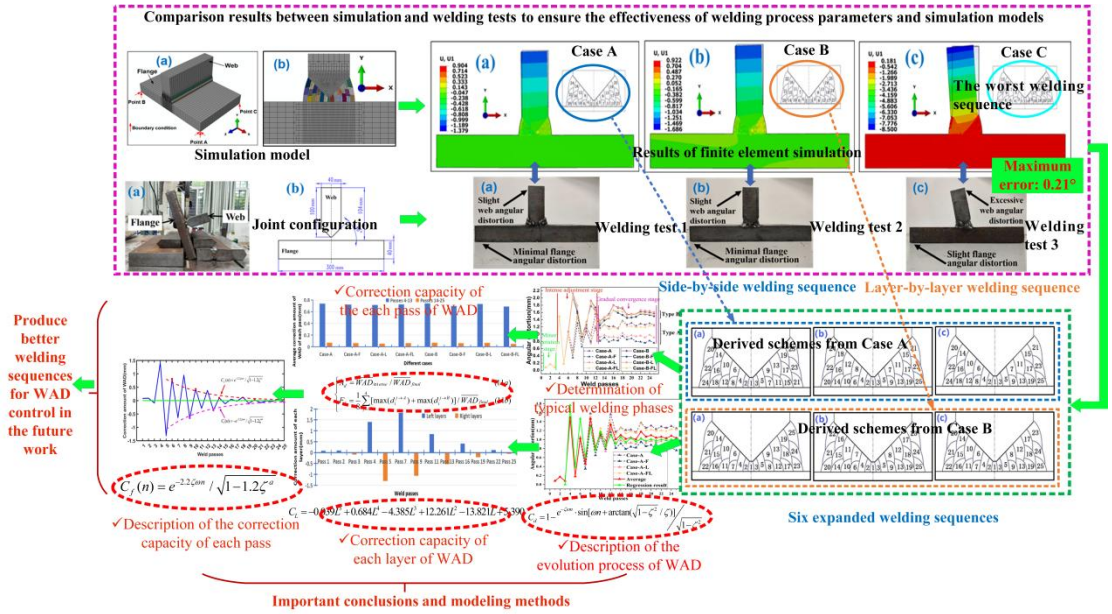


Fig. 5 Graphical abstract of the following research contents.

3. Numerical analysis

The FE software ABAQUS is employed to simulate the temperature field, angular distortion, and welding residual stress, using a sequentially coupled thermal-mechanical approach. A geometric model is created, which matches the dimensions of the actual welded specimen. The FE mesh is generated prior to analysis and computation.

The simulation process consists of two stages. In the thermal analysis stage, the temperature distribution during welding is first calculated independently. The material properties are defined as temperature-dependent functions based on experimental data. An appropriate element type is selected to meet thermodynamic analysis requirements. The heat input model is defined according to welding parameters. Initial conditions and heat dissipation boundary conditions are applied,

followed by thermal analysis to determine the transient temperature history at each node. In the mechanical analysis stage, the computed temperature field is imported as a thermal load into the mechanical model. The mechanical properties (e.g., yield strength, elastic modulus) of the material are specified as temperature-dependent functions, and a suitable element type is chosen for structural analysis. After applying mechanical boundary conditions, the model is solved to obtain the residual stress distribution and angular distortion of the welded specimen.

3.1. FE model and simulation cases

Figure 6 shows the FE model of the thick plate T-joint used in this study. To isolate the effects of welding sequences on WAD and residual stress, all models maintain identical geometric dimensions and weld bead morphology, with variations only in the heat input sequence. Minor differences in weld bead morphology between welding cases were considered negligible and thus not modeled.

The model features a non-uniform mesh configuration that balances computational accuracy with efficiency. A fine mesh is employed in the weld zone and adjacent heat-affected zone, while a coarser mesh is used in regions farther from the weld. The complete model consists of 62,475 elements, with DC3D8 elements for temperature field analysis and C3D8I elements for stress-strain field analysis.

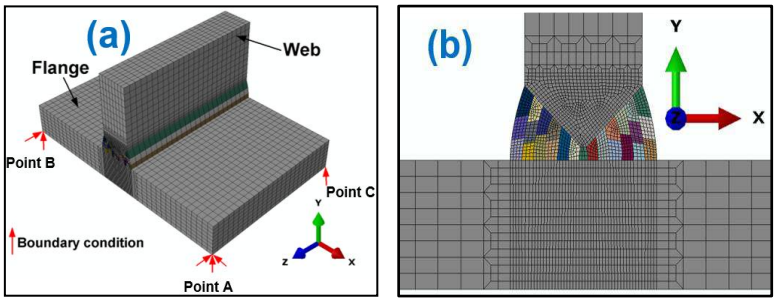


Fig. 6 FE model of the T-joint. (a) Free boundary condition. (b) Illustration of weld passes.

3.2. Thermal analysis

During the welding process, the thermophysical and mechanical properties of the material typically vary with temperature. Consequently, the nonlinear behavior of material properties must be accounted for in numerical simulation. The thermophysical property parameters of Q345D steel and ER50-6 [37] are presented in **Fig. 7**.

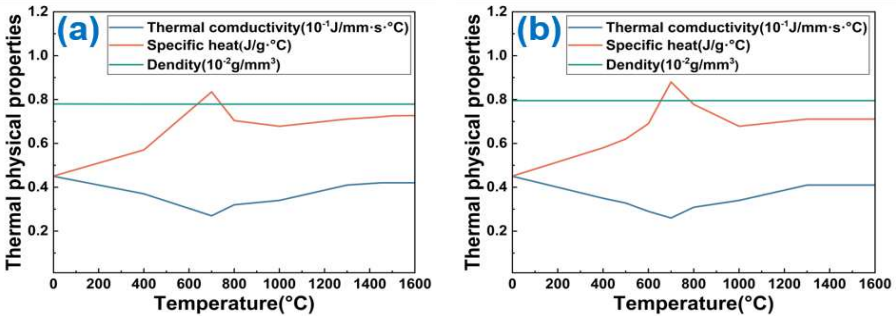


Fig. 7 Temperature-dependent thermal physical properties of (a) Base material and (b) Welding wire.

The welding heat source serves as the foundation for simulating the welding thermal process. To accurately model the welding process with varying heat inputs, this study adopts the double ellipsoid heat source model proposed by Goldak [38]. The model divides the heat source into front and rear halves, each with distinct heat flux density distributions. Equation (2) defines the heat flux density distribution function for the front half of the heat source, while Equation (3) describes the corresponding function for the rear half.

$$q(x,y,z,t)=\frac{6\sqrt{3}f_f Q_w}{\pi a_f bc\sqrt{\pi}}e^{-3(x/a_f)^2}e^{-3(y/c)^2}e^{-3(z/d)^2} \tag{2}$$

$$q(x,y,z,t)=\frac{6\sqrt{3}f_r Q_w}{\pi a_r bc\sqrt{\pi}}e^{-3(x/a_r)^2}e^{-3(y/c)^2}e^{-3(z/d)^2} \tag{3}$$

where Q_ω represents the total heat, a_f, a_r, c, and d are the shape parameters of the double ellipsoid in the X-, Y- and Z-directions, respectively, f_f and f_r respectively denote the front and rear heat distribution functions, with $f_f + f_r = 2$. In this research, the parameters are set as $f_f = 0.6$ and $f_r = 1.4$. The nonlinear transient heat transfer equation is given as Eq. (4), which must be solved to determine the temperature cycle during the welding process:

$$\rho C\frac{\partial T}{\partial t}(x,y,z,t)=-\nabla\vec{q}(x,y,z,t)+Q(x,y,z,t) \tag{4}$$

where ρ represents the mass density, C is the specific heat capacity, q is the heat flux, and Q denotes the heating rate of the internal heat source. The law of heat conduction by Fourier is applied to describe the heat conduction process of arc heat in the welded specimen. The conduction equation is:

$$\vec{q}=-kT \tag{5}$$

where k represents the temperature-dependent thermal conductivity. The law of cooling by Newton is applied to account for convective heat dissipation from weldments:

$$q_c=-h_c(T_s-T_0) \tag{6}$$

where h_c denotes the convection heat dissipation coefficient, set to 15×10^{-6} W/(mm^2·°C), T_s is the surface temperature of the workpiece, and T_0 represents the ambient temperature. The ambient temperature is considered to be 20 °C, based on the room temperature during actual welding. Radiant heat loss is considered using Boltzmann's law:

$$q_r=-\varepsilon\sigma[(T_s+273)^4-(T_0+273)^4] \tag{7}$$

where ε represents the thermal emissivity (set to 0.85 in this study), and σ is the Stefan-Boltzmann constant (5.67×10^{-14} W·mm^{-2}·°C^{-4}). Additionally, the latent heat of crystallization of the melt pool is considered in the welding heat process. For Q345D, the latent heat is 300 J/g, and the liquids and solidus temperatures are 1480 °C and 1430 °C, respectively.

3.3. Mechanical analysis

Throughout the welding process, no additional constraints are applied to the weldment. The mechanical boundary conditions restrict displacements at only three nodes, as illustrated in **Fig. 6a**.

- **Point A** constrains all three translational degrees of freedom (X, Y, and Z-directions).
- **Point B** restricts movement in the X and Z-directions.
- **Point C** fixes the Z-direction displacement.

These constraints prevent rigid-body motion and rotation of the weldment.

The mechanical analysis uses the same mesh model as the thermal analysis. Thermal results are applied as thermal loads. They are used in the thermal-elastic-plastic FE model. This model computes welding-induced stress and distortion. Since creep and solid-state phase transformation have negligible effects on angular distortion and residual stress, they are disregarded. Accordingly, the total material strain is expressed as:

$$\varepsilon_{total} = \varepsilon_e + \varepsilon_p + \varepsilon_{th} \tag{8}$$

where ε_e, ε_p, and ε_{th} are the elastic strain, plastic strain, and thermal strain, respectively.

During the mechanical analysis, the elastic strain at each material point is modeled using the isotropic Hooke's law, while plastic behavior is governed by the Von Mises yield criterion. The thermal strain is computed based on the coefficient of thermal expansion, and work hardening effects are neglected. The temperature-dependent mechanical properties of the material [37] are illustrated in **Fig. 8**.

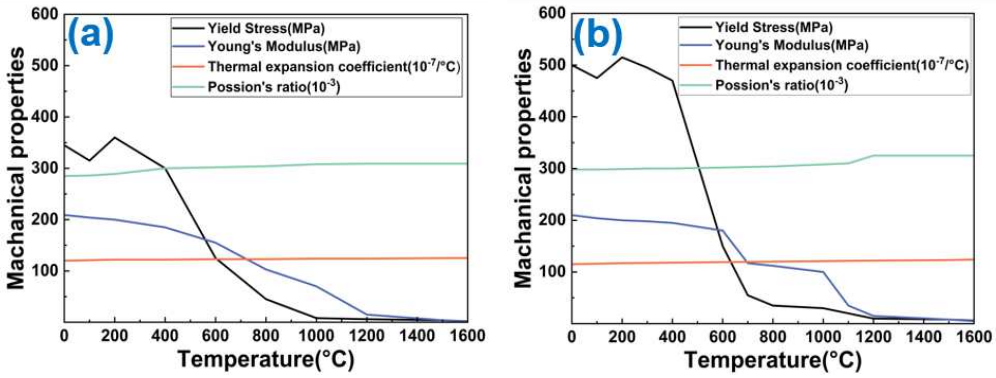


Fig. 8 Temperature-dependent mechanical properties of (a) Q345 and (b) ER50-6.

4. Results and discussion

4.1. Comparison of numerical simulation and welding results

Prior to a comprehensive investigation of angular distortion evolution using numerical simulation, the accuracy of the proposed FE method was validated by comparing simulation results with welding tests. The welded specimens (**Fig. 9**) of Cases A-C reveal significant variations in WAD due to different welding sequences. In contrast, flange distortion remains relatively minor when the flange thickness exceeds 30 mm, indicating that primary attention should be directed toward WAD.

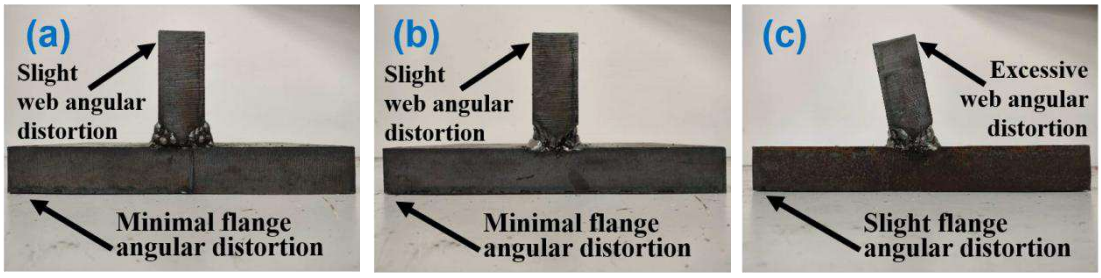


Fig. 9 Welding results with three welding sequences corresponding to (a) Case A, (b) Case B, and (c) Case C in Fig .3.

The T-joint fabricated under Case A exhibits satisfactory weld morphology, as shown in **Fig. 10**. To further verify the effectiveness of the welding parameters and method, macro-metallographic analysis was performed on the welded joint (**Fig. 11**) after etching in a 4% nitric acid alcohol solution. The results confirm there are no macroscopic welding defects. These include cracks, pores, slag inclusions, and incomplete fusion. This demonstrates the selected welding heat input parameters are suitable. This quality assessment further supports the reliability of the numerical simulation results.



Fig. 10 As-deposited weld morphology with welding sequence Case A. (a) Macroscopic morphology. (b) Lateral view of the fusion zone. (c) Planar view of the fusion zone.

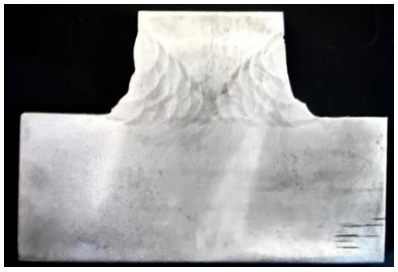


Fig. 11 Macro metallography of the welding joint.

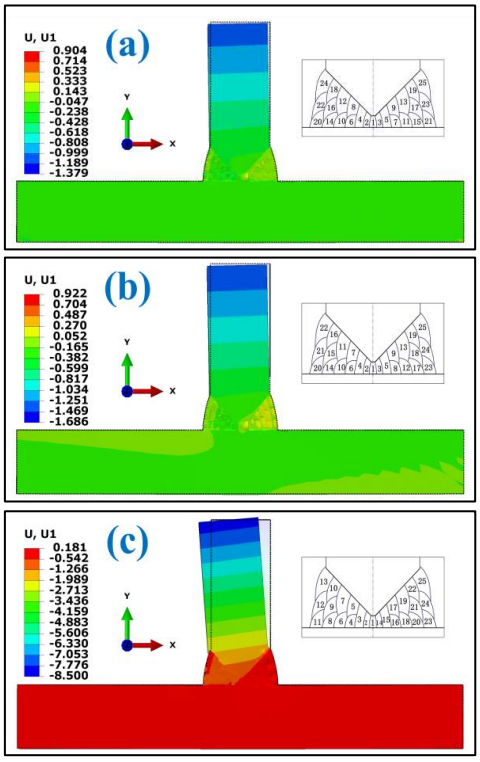


Fig. 12 Contour plots of simulated joint distortion corresponding to (a) Case A, (b) Case B, and (c) Case C.

Figure 12 illustrates the *X*/*Y*-direction views of simulation results for the three cases. The wireframe represents the initial model geometry before welding, while the color-filled geometry depicts the post-welding WAD. In ABAQUS, displacement variation in the *X*-direction is denoted by U_1. The WAD in the simulation result is quantified by measuring the change in U_1 at the top of the web.

In thermal field simulation, the arc heat input process is modeled using a moving heat source. The welding direction remains consistent for all welds, resulting in a peak temperature that progressively increases from the starting position of the heat source along the *Z*-direction. This temperature gradient leads to a gradual increase in WAD along the welding direction in the mechanical field simulation. The WAD along the welding direction is approximately linear with a slight increase, as illustrated in the third perspective view of Case A in **Fig. 13**, where the uneven U_1 of the web are evident.

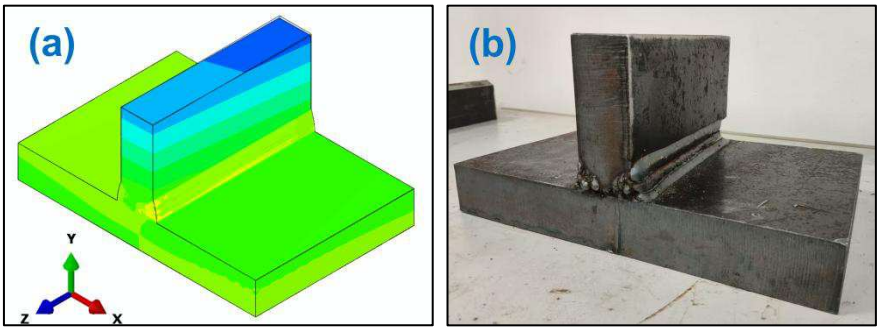


Fig. 13 The third angle of view of the WAD of Case A. (a) Simulation result. (b) Welding result.

In actual welding, uneven WAD was also observed. It typically shows smaller values near the initial welding position and larger values near the arc termination position. This behavior is partly attributed to the preheating effect, provided by the initial weld on subsequent regions. The simulated displacement (**Fig. 14**) shows that the value of the midpoint node is approximately equal to the average value of all nodes, across the three welding sequences. Since this study focuses on comparing the effects of different welding sequences, including numerous similar data points would unnecessarily complicate the analysis. Given that the simulated angular distortion along the *Z*-direction approximately follows a linear trend, the midpoint at the top of the first-welded side is selected as the representative data point.

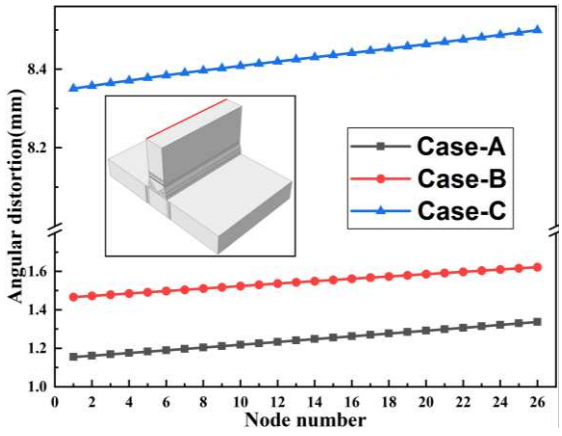


Fig. 14 The angular distortions of each node on the first welding side of the top of the web, from the three welding sequences.

The statistical results (**Table 3**) show that both single-pass alternating and layer-by-layer welding sequences reduce WAD by over 80% compared to the fully-welded one-sided sequence. Additionally, the angular distortion reduction achieved by the single-pass alternating sequence is 17% greater than that of the layer-by-layer alternating sequence.

Table 3

Comparison of the final WADs by the three welding sequences.

Case	Experiment (mm)	FEM (mm)
A	1.38	1.25
B	1.66	1.57
C	8.78	8.41

The corresponding simulation results are relative errors of 9.4%, 6.6%, and 4.1%, compared to experimental results respectively. The maximum error of WAD between simulation and welding results is 0.21° . As shown in **Figs. 9** and **12**, the WAD subjected to multi-layer and multi-pass welding is markedly greater than that of the flange. The magnitude of WAD varies substantially across welding sequences. These results clearly confirm that optimized welding sequences can effectively control WAD.

The differences of the evolutionary process of WAD between the simulation and welding results (**Fig. 15**) further ensure the effectiveness of the proposed FE method here. In addition, these results display significant fluctuations of WAD in different welding stages. They characterize three significant evolution stages, minor variation, intense adjustment, and gradual convergence stage. These findings are further validated and modeled in the next section.

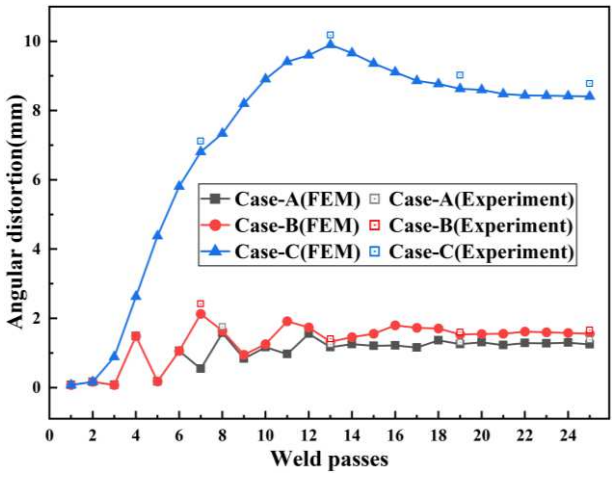


Fig. 15 Comparison of the evolutionary process of WAD between the simulation and welding results, and differences in WAD caused by different welding sequences.

In addition, in Case A maximum WAD (1.58 mm) was recorded upon completion of the eighth weld pass, which exhibits enhanced stability of cumulative distortion compared to other cases. In Case B, WAD decreases gradually as alternating groove filling progresses, peaking at 2.13 mm after the seventh weld pass with higher curve irregularity. In Case C, welding of the opposite groove commences only after full completion of one groove side, thereby inducing a cumulative process of WAD characterized by an initial rapid rise followed by a decline. After the first 13 weld

passes, WAD peaks at 9.90 mm. Throughout the subsequent 12 passes, despite steady distortion reduction, this subsequent stage provided a mere 1.49 mm correction, yielding a residual angular distortion of 8.41 mm in the final state.

The angular distortion induced by individual weld passes is quantified (**Fig. 16**), to further understand the cumulative change in WAD. Larger angular distortions are primarily concentrated between the fourth and 13th passes. During the first three passes, the low heat input and central welding position within the groove result in minimal angular distortion along the web's left and right offsets. From the fourth pass onward, as the welding position shifts outward and heat input increases, the angular distortion induced by individual weld beads begin to rise. The maximum angular distortion change, 1.41 mm, occurs during the fourth pass.

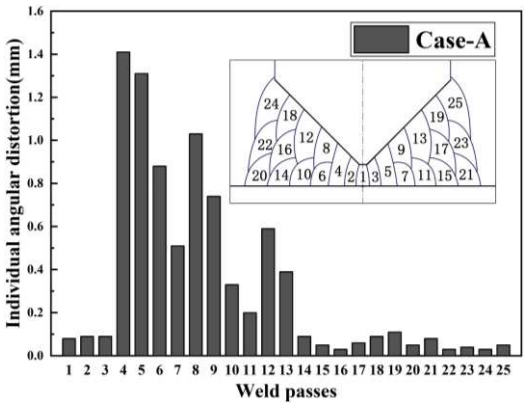


Fig. 16 Individual angular distortion along with passes in Case A.

Further analysis indicates that between the fourth and 15th weld passes, the WAD on the first side of the groove is consistently greater than that on the second side, e.g., the sixth weld pass exceeds the seventh one, and the eighth weld pass exceeds the ninth one. The reason is that in the early stages of welding, the joint exhibits low stiffness, allowing the web to shift easily under the contraction forces of the weld passes. As the number of weld passes increases, the joint stiffness improves, reducing the plate tendency to shift.

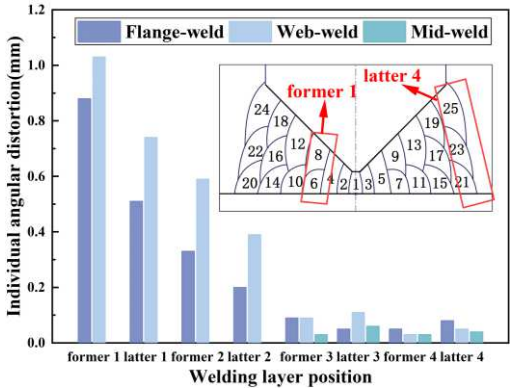


Fig. 17 Individual WAD of the weld pass at different positions in the same welding layer.

When comparing the magnitude of WAD at different locations within the same welding layer, it is observed that the influence of spatial position on WAD exhibits significant variations. As shown in **Fig. 17**, the sixth and eighth weld passes are grouped into a welding layer termed "*former* 1", the 10th and 12th weld passes into "*former* 2", the seventh and ninth weld passes into "*latter* 1",

and the 21st, 23rd, and 25th weld passes into "*latter* 4", with other welding layers similarly named. Weld passes near the flange are classified as Flange-welds, those near the web as Web-welds, and those in intermediate positions as Mid-welds. By examining the WAD changes caused by weld passes at different positions within the same layer, it is evident that the WAD induced by Flange-welds is consistently smaller than that of Web-welds in *former* 1, *former* 2, *former* 3, *latter* 1, *latter* 2, and *latter* 3. Conversely, the opposite trend is observed in *former* 4 and *latter* 4, likely due to increased joint stiffness and the impact of stresses on both sides.

Similar to Case A, weld passes on the first welding side in Case B exhibit greater distortion alteration capacity than those on the second side (**Fig. 18**). Additionally, the Web-welds cause more distortion than the Flange-welds within the same welding layer.

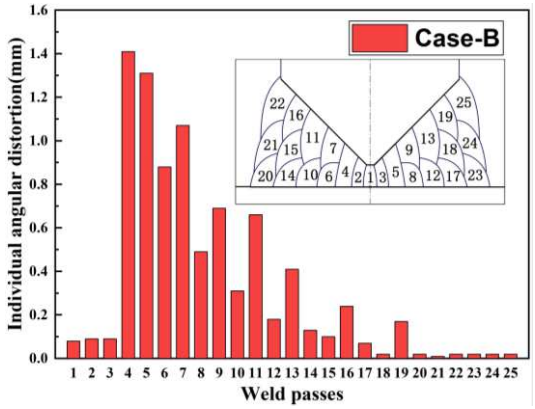


Fig. 18 Individual WAD of each weld pass in Case B.

In Case C (**Fig. 19**), a significant difference in joint stiffness between the corresponding positions on both sides of the bevels is observed. Here, the WAD changes on the first welding side are consistently larger than those on the second side. However, unlike Cases A and B, the distortion caused by the Web-welds is not consistently greater than that of the Flange-welds. In addition, the WAD evolution from the first to 13th weld passes follows an initial increase-peak-decay pattern, excluding negligible fluctuations at the ninth/12th Mid-welds.

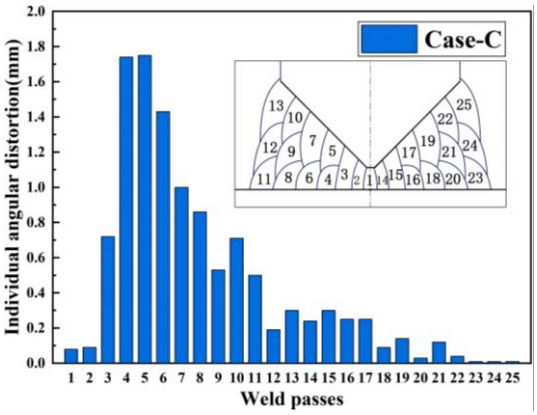


Fig. 19 Individual WAD of each weld pass in Case C.

4.2. Evolution characteristics of WAD by welding sequences

To further investigate the influence of welding sequences on WAD and evolution characteristics, six expanded welding sequences are considered based Cases A and B, as depicted in **Figs. 20** and

21. The three cases depicted in **Fig. 20** are from Case A and classified as Type A. The distinction among the three cases lies in the welding order. In Case A-F, the same-layer weld bead on the groove of the initial welding side starts from the web side, while the subsequent groove starts from the flange side. Conversely, in Case A-L, the initial groove is welded from the flange side, while the subsequent groove begins near the web side. In Case A-FL, welding starts from the web side each time. In **Fig. 21**, Cases B-F, B-L, and B-FL are from Case B and are classified as Type B, which are based on the alternated interlayer welding process, with single-layer deposition on one side immediately followed by counter-side welding.

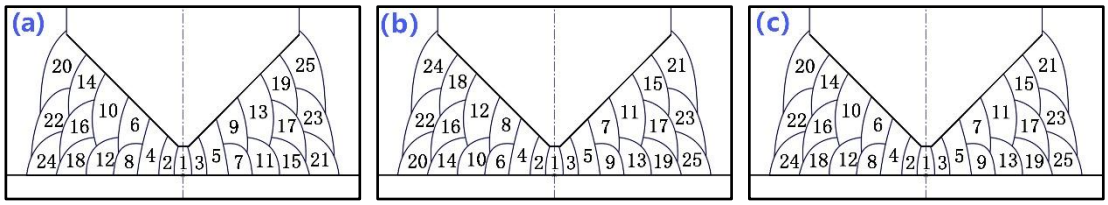


Fig. 20 Three welding sequences derived from Case A, respectively named (a) Case A-F, (b) Case A-L, and (c) Case A-FL.

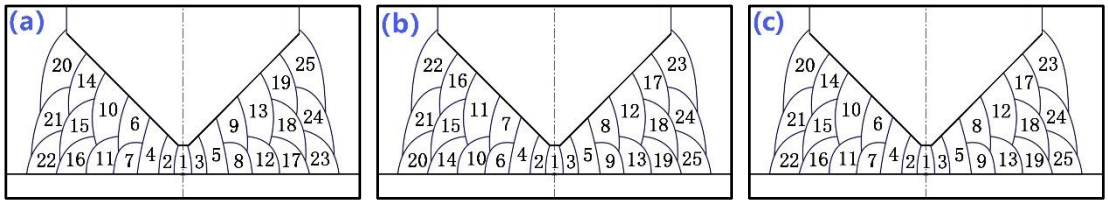


Fig. 21 Three welding sequences derived from Case B, respectively named (a) Case B-F, (b) Case B-L, and (c) Case B-FL.

Some definitions are given before the analysis of evolution characteristics. $d_i^{j\to A}(j=1,2,\cdots 4; i=1,2,\cdots 25)$ represents the WAD of each pass in Type A and Case A, where $j(j=1,2,\cdots 4)$ is used to denote the four cases respectively. $d_i^{j\to B}$ thus denotes the corresponding distortion in Type B and Cases B. Let Δd_k^j be the correction amount of WAD in two adjacent passes, and Δd_k^j is computed as

$$\Delta d_k^j = d_k^j - d_{k-1}^j \tag{9}$$

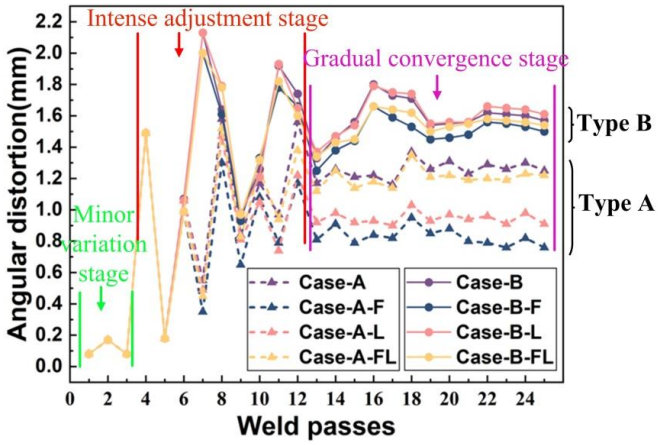


Fig. 22 Evolution processes of WAD among the eight welding sequences.

The results (**Fig. 22**) highlight three evolution stages. In the intense adjustment stage covering the 4th–13th weld passes, WAD intensely fluctuates with a trend of gradual convergence. Let $\overline{WAD}_{\text{int}ense}$ denote the average WAD across the eight cases during this stage, and $\overline{WAD}_{final}$

represent the final average WAD as Eq. (10). The accumulative degree A_d and fluctuation degree F_d are defined by Eq. (11), respectively. Here, $A_d = 0.9$ and $F_d = 1.4$. The value of 0.9 suggests a potential reduction in WAD during subsequent welding. In Type A, this stage spans 10 weld passes, accounting for 40% (10/25) of the total passes.

$$\begin{cases} \overline{WAD}_{\text{int}ense} = \dfrac{1}{4}\sum_{j=1}^{4}\dfrac{1}{10}\sum_{i=4}^{13}\dfrac{1}{2}(d_i^{j\to A} + d_i^{j\to B}) & (10a) \\ \overline{WAD}_{final} = \dfrac{1}{4}\sum_{j=1}^{4}\dfrac{1}{2}(d_{25}^{j\to A} + d_{25}^{j\to B}) & (10b) \end{cases} \tag{10}$$

$$\begin{cases} A_d = \overline{WAD}_{\text{int}ense} / \overline{WAD}_{final} & (11a) \\ F_d = \dfrac{1}{8}\sum_{j=1}^{4}[\max(d_i^{j\to A}) + \max(d_i^{j\to B})] / \overline{WAD}_{final} & (11b) \end{cases} \tag{11}$$

Second, the gradual convergence stage comprises the final 12 weld passes, accounting for 48% of the total. In this stage WAD variations diminish, indicating substantial stiffness. Here, $A_d = 1.02$ and $F_d = 1.12$, both confirms the stabilization of WAD.

In contrast, the minor variation stage generally covers the first three passes. This stage is characterized by low heat input. It contributes less than 0.52° of distortion. This amount is under 8% of the total. Notably, this stage is absent in [32] due to the differences in the welding sequences of the first three passes, compared to this study.

The final WAD of Type A is consistently lower than those of Type B, which shows that the alternating welding sequence on both sides provides better WAD control. On average, Type B exhibits about 1.5 times higher WAD than Type A (**Table 4**). Notably, Type B shows relatively uniform final WAD with fewer fluctuations during the intense adjustment stage, compared to Type A.

The minimum WAD occurs in Case A-F. In this case, the first side employs the in-layer sequence starting with the web side. This configuration achieves a WAD of 0.76 mm (0.44°). This value represents a 39.2% reduction compared to the final WAD of Case A. In contrast, Type B demonstrates minimal variability, with a maximum final WAD difference of only 0.11 mm.

Table 4

Comparison of the final WAD using the eight welding sequences.

Type A	*U*1 (mm)	Type B	*U*1 (mm)
Case A	1.25	Case B	1.57
Case A-F	**0.76**	**Case B-F**	**1.50**
Case A-L	0.91	Case B-L	1.61
Case A-FL	1.22	Case B-FL	1.54

To quantitatively compare the distortion correction effects between the last two stages, $\left|\Delta d_k^j\right|$ is used as the correction metric. For each case, the average correction amount can be expressed as $\sum_{k=1}^{25}\left|\Delta d_k^j\right| / 25$. As shown in Fig. 23, the correction effect differs significantly between stages. The ratio is 69:5. This demonstrates that welding sequence optimization should focus primarily on the intense adjustment stage. Such focus is necessary for effective WAD control.

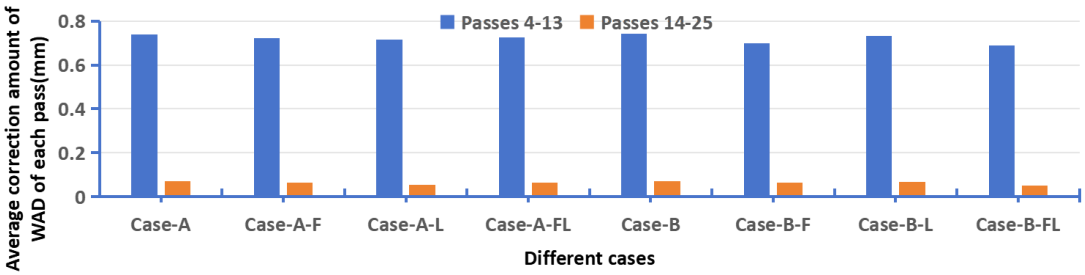


Fig. 23 Comparison of the distortion correction amount between the last two stages.

In Type A, variations in the magnitude of WAD arise among individual welds. These variations are caused by differences in welding sequences across the four cases. The sequences lead to distinct cumulative trends. Cases A and A-FL, which employ symmetrical welding sequences on both sides, exhibit comparable WAD magnitudes but worse overall results. In contrast, the asymmetric and diagonally intersecting sequences in Cases A-F and A-L yield lower WAD.

After the sixth weld pass, the cumulative WAD in Case A-F becomes lower than in the other cases, with further distortion correction occurring during the seventh weld. By the completion of the eighth and ninth welds (i.e., the *former* 1 and *latter* 1 weld layers), the cumulative WAD in Case A-F is approximately 0.2 mm lower than in the other cases.

Notably, Case A-F delivers the best results. This outcome is due to its strategy. The strategy welds the web side first. It also employs a diagonally intersecting sequence. This sequence applies to two corresponding welding layers. These layers are on both sides of the web. This approach demonstrates superior distortion correction capability, as illustrated in **Fig. 24**. The correction effect exhibits an attenuation trend with successive weld passes. Two regression equations, shaped like enveloping curves, are formulated to quantify the correction laws for weld passes on both sides of the joint as:

$$C_f(n) = e^{-2.2\zeta\omega n} / \sqrt{1-1.2\zeta^a} \tag{12}$$

$$C_l(n) = -e^{-2.2\zeta\omega n} / \sqrt{1-1.2\zeta^b} \tag{13}$$

where n represents weld passes, and $C_f(n)$ and $C_l(n)$ represents correction magnitude of WAD respectively belong to the passes that locates at the two web side. The related parameters are set as $\omega = 3.14$, $\zeta = 0.023$, $a = 0.15$, and $b = 0.10$, through numerical analysis.

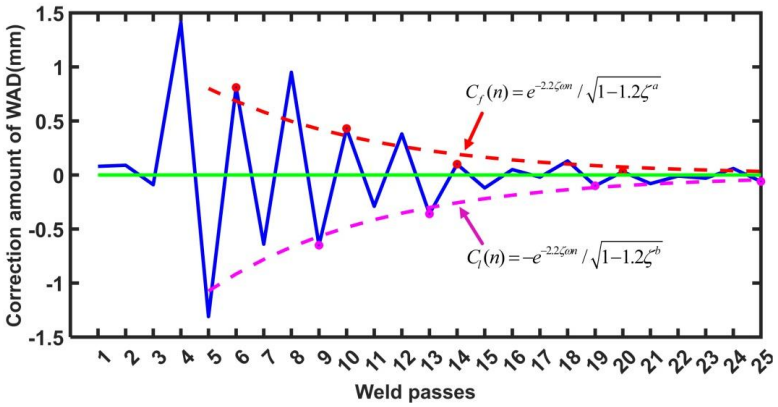


Fig. 24 The distortion correction capacity of different weld passes in Case A-F, where red dots represent the passes of the first welding side and pink dots denote the passes of the other side. The MSEs of upper and lower regression results are 0.115 mm^2 and 0.108 mm^2.

In [30], two welding sequences, the web-side-first and flange-side-first, were compared in terms of their WAD control effectiveness. The study concluded that the flange-side-first approach provides better WAD control, which appears to contradict our findings. However, this discrepancy may arise from differences in groove configurations (single V-groove vs. double V-groove) between the two studies.

Nonlinear regression modeling based on the minimum variance criterion is used to analyze the cumulative characteristics of WAD in Type A (**Fig. 25**). The resulting description function is given in Eq. (14). This function is analogous to the unit step response of a second-order linear system. It can serve as a corrective reference for optimizing welding sequences. The optimization involves alternating passes on both sides of the web.

$$C_d = 1 - e^{-\zeta\omega n} \cdot \sin[\omega n + \arctan(\sqrt{1-\zeta^2}/\zeta)] \Big/ \sqrt{1-\zeta^2} \tag{14}$$

where C_d represents the cumulative WAD, and n denotes weld passes. The related parameters are set as $\omega = 3.14$ and $\zeta = 0.078$.

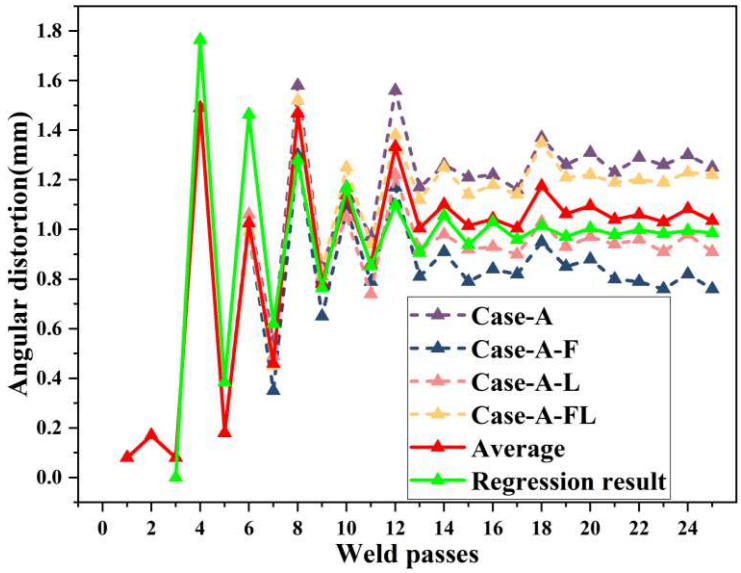


Fig. 25 Accumulative change process of WAD of Type A and the regression result, where the MSE of the regression model is 0.088 mm^2.

Type B welding sequences (**Fig. 22**) exhibit smaller variations in the gradual convergence stage. Among these, Case B-F shows the flattest evolution curve and the smallest WAD, while Case B-L demonstrates significantly higher distortion progression, reaching the maximum WAD. However, the cumulative patterns of WAD generated by these four welding sequences are very similar, and the difference in final WAD is not significant.

A comparison between Case B and B-FL (**Fig. 26**) reveals that the designed welding sequences weaken the effect of single-layer alternating on WAD.

Since Case B-F yields the best WAD control result in Type B, the optimal welding sequence is reaffirmed as web-side-first with diagonally-intersecting welding. Unlike the pattern in **Fig. 24**, the key distinction here lies in applying diagonal intersection by welding layers, as demonstrated through two WAD correction analyses (**Figs. 27** and **28**) based on Case B-F.

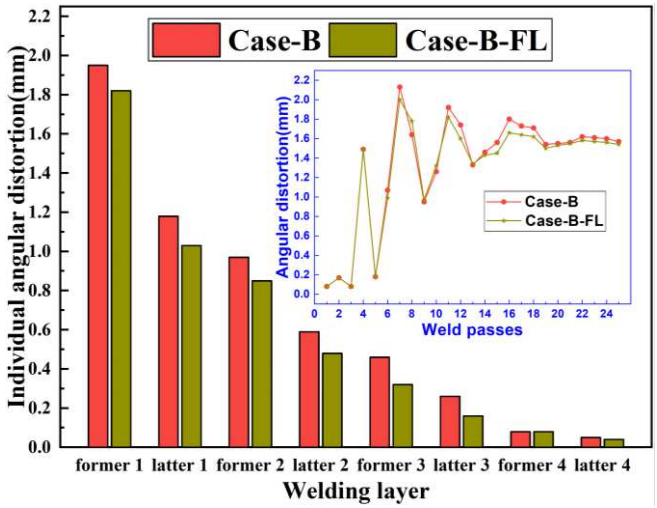


Fig. 26 Individual angular distortion of each welding layer.

The regression model of correction amount of WAD in the layer-by-layer mode is built through 5th-order higher-degree equation as:

$$C_L = -0.039L^5 + 0.684L^4 - 4.385L^3 + 12.261L^2 - 13.821L + 5.390 \quad (15)$$

where C_L represents the correction amount of WAD of each welding layer, and L denotes the welding layer.

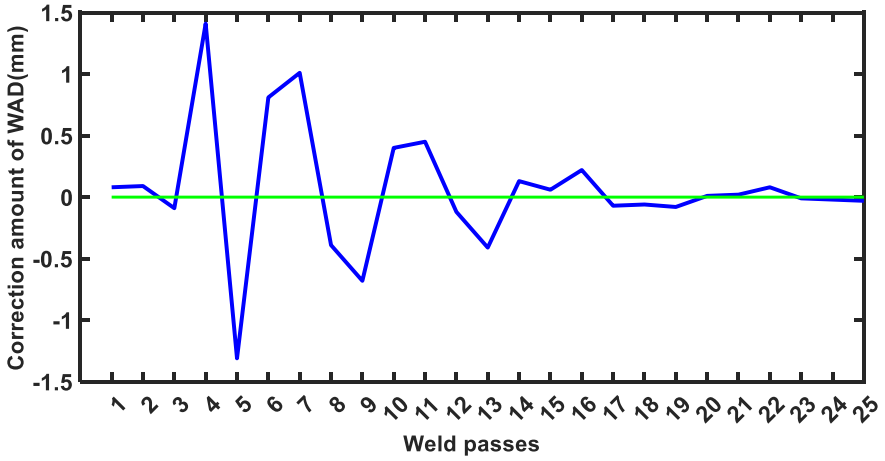


Fig. 27 Example of correction amount of WAD in the mode of pass-by-pass, using Case B-F.

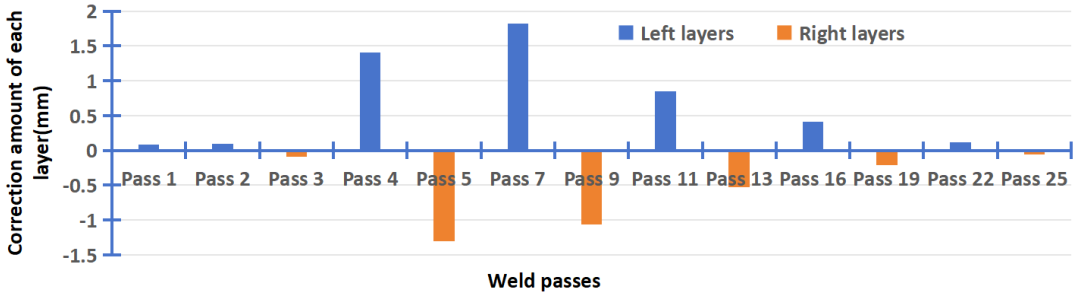


Fig. 28 Example of correction amount of WAD in the mode of layer-by-layer using Case B-F, where "Left layers" means the first side to be welded, and there is a welding layer from Pass 5 to 7, for example.

Compared to [33], the WAD evolution patterns differ significantly during the rapid cumulative stage. This discrepancy arises from differences in welding sequences, base materials, and the

number of weld passes. Since our study involves far more weld passes, the oscillation degree in this stage is more pronounced. Despite these differences, two key similarities emerge between the studies: (1) WAD increases rapidly during the cumulative stage. (2) WAD fluctuations gradually stabilize in the final passes.

From experimental and FE simulation results, several critical WAD evolution laws can be summarized: (1) There are two distinct evolution stages, intense adjustment and gradual convergence phases. The intense adjustment stage is characterized by rapid growth with large oscillations, while the gradual convergence stage works with minor oscillations approaching a steady state. These findings are also confirmed by [30]. These stages are clearly demarcated by the percentage of completed weld passes, regardless of whether single-pass or single-layer diagonally-intersecting welding is used. (2) Single-pass diagonal (e.g. Case A-F) welding provides better WAD control than single-layer diagonal (e.g. Case B-F) welding. However, its welding efficiency is lower due to frequent side switching. It is control effectiveness vs. efficiency. (3) Completing one side before switching to the other (Case C) yields the worst control result. (4) The cumulative behavior in the early welding phase is highly welding sequence-dependent. WAD optimization rules involve three points, namely adopting a pass-alternated welding sequence, prioritizing one-side web welding first and the other-side base plate welding subsequently, and increasing the frequency of alternating welding on both sides during the adjustment phase.

4.3. Residual stress distribution

In the *X*-direction at the central cross-section of the weld, the residual stress distribution exhibits similar characteristics under Cases A, B, and C, as shown in **Fig. 29**. High tensile stress regions are located at the weld toe on the flange and the center of the flange surface, while significant compressive stresses are observed in the central area of the flange. Notably, the residual stress distributions of Cases A and B demonstrate considerable symmetry. The peak residual stresses at the weld toe are 361 MPa and 370 MPa, respectively, both exceeding the peak residual stress of Case C (337 MPa). Additionally, the high-stress area on the side welded first in Case C is significantly smaller compared to the side welded last.

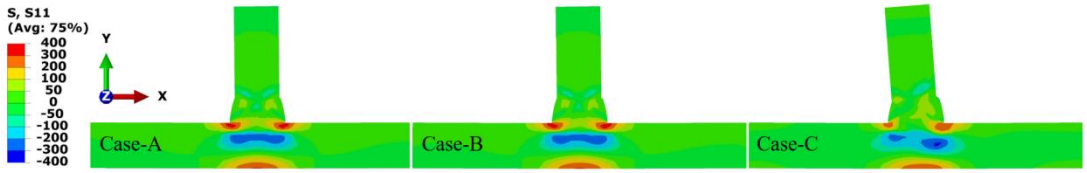


Fig. 29 Stress distribution of Case-A, Case-B, and Case-C in the *X*-direction.

In the *Y*-direction as shown in **Fig. 30**, high-stress concentrations are predominantly located in the weld region, and the stress distribution alternates between tensile and compressive stresses. In Cases A and B, the regions of high tensile stress are concentrated in the last two weld metal layers and at the weld toe. The residual stresses on the first and last welded sides exhibit approximate symmetry. The peak tensile stresses for Cases A and B are 356 MPa and 375 MPa, respectively. The average peak tensile stress of Cases A and B differs only by about 5 MPa from the average value generated by the three welding sequences in [30], even though the joint in this paper is a K-groove and the joint in [30] is a single V-groove. In contrast, Case C shows distinct stress distribution patterns, with high tensile stress areas concentrated near the cover plate weld zone on

the first welded side and at the weld toe of the last flange layer. Notably, the peak tensile stress on the first welded side reaches 413 MPa, while the last welded side only reaches 343 MPa. Cases A and B exhibit extensive compressive stresses at the blunt edge of the web, whereas Case C shows a bias toward compressive stresses near the weld area on the first welded side.

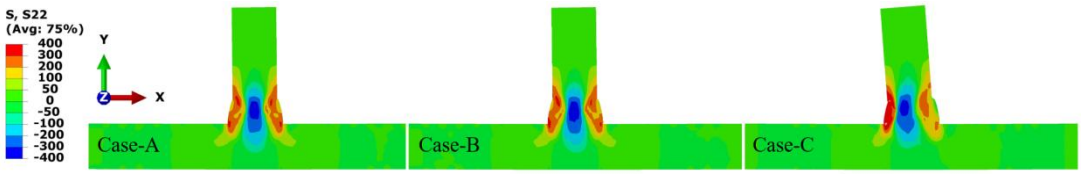


Fig. 30 Stress distribution of Case-A, Case-B, and Case-C in the *Y*-direction.

The residual stress distribution in the *Z*-direction (**Fig. 31**) alternates distinctly between tensile and compressive stresses within the weld zone. The residual stress distributions in Cases A and B remain largely symmetric, with peak tensile stresses around 460 MPa for all three cases. In Case C, the majority of high tensile stress is concentrated in the weld zone on the last welded side, whereas the high tensile stress area on the first welded side is limited to the outer toe of the bevel between the web and the flange.

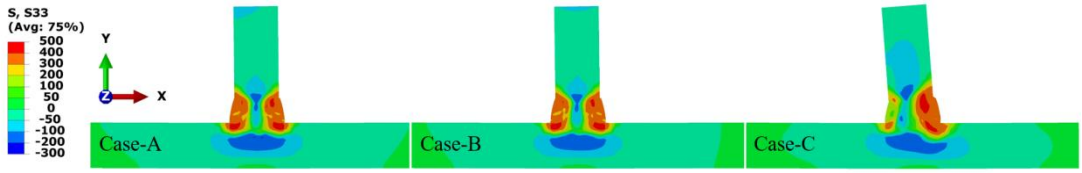


Fig. 31 Stress distribution of Case-A, Case-B, and Case-C in the *Z*-direction.

4.4. Comprehensive evaluation of welding sequences

The comparative analysis reveals distinct performance characteristics among the welding sequences. Under Case A-F, WAD is minimal, and the high tensile stress distribution area is the significantly smallest, making it suitable for applications requiring minimal welding angular distortion and residual stress. The layer-by-layer welding method in Case B also effectively reduces WAD and offers greater welding efficiency. Conversely, Case C results in substantial WAD and a broader distribution of high tensile stress. This welding sequence is not therefore recommended.

5. Conclusion and future work

This paper investigated the evolution characteristics of WAD of 40 mm thick plate T-joint with the K-groove via numerical simulation and statistical regression modeling, considering pass-by-pass and layer-by-layer welding sequences. Several conclusions about evolution laws of WAD and optimal welding sequences are made as follows.

(1) Whether the alternating welding is performed in a pass-by-pass or layer-by-layer manner on both sides of the web, the evolution of WAD exhibits two distinct stages. The first is the adjustment stage characterized by intense oscillations. The second is the gradual stabilization stage marked by convergence. The proportion of weld passes in each stage is approximately 40% and 48%, respectively. This means that in order to achieve better control of WAD, a more optimal pass planning strategy should be developed for the first 40% of weld beads.

(2) In alternating welding performed in the pass-by-pass and layer-by-layer manner, prioritizing one-side web welding first and the other-side base plate welding subsequently, referred to as the diagonally-intersecting welding sequence, proves more effective in controlling WAD.

(3) Under the premise of single-robot welding, adopting a pass-alternated welding sequence during the intense adjustment stage is recommended, combing with a layer-alternated approach in the gradually stabilizing convergence stage. This strategy effectively balances the control of WAD with welding efficiency.

(4) The evolution processes of WAD using the pass-by-pass or the layer-by-layer welding sequence can be modeled by a Sine-Exponential function. Also, the WAD correction capacities of each pass and layer can be understood with the exponential function and the quintic equation, respectively. These models can be used for predicting WAD.

(5) It is not suggested to complete welding on one side of the web and then proceed to weld the other side, because this welding sequence definitely not yield the good control effect of WAD.

In future work, we will further verify whether the first point in conclusion remains valid for T-joints of different thicknesses, and confirm the proportion of weld passes at each stage. Meanwhile, based on *Conclusion* (3), we will further consider the welding sequence to achieve better control effects on WAD, thereby developing a universal weld planning strategy for angular distortion control in GMAW of T-joints with K-grooves. These strategies proposed in this paper should also be applied to T-joints of other thicknesses to verify their effectiveness.

Funding sources:

This work was supported by the National Natural Science Foundation of China under grants 62066029 and by the 2026 Special Research Project for Teachers “Capacity Improvement” under grant Ncjt-20260306.

Declaration of interests:

The authors declare that they have no known competing financial interests or personal relationships that could have appeared to influence the work reported in this paper.

Contribution declaration:

Zhuohua Yu: Conceptualization, Methodology, Investigation, Formal analysis, Writing – original draft.

Xiaomin Liu: Software, Project administration, Conceptualization.

Junpei Deng: Resources, Validation, Investigation, Writing – review and editing.

Yimeng Xie: Investigation, Visualization, Data curation.

Yaqi Sun: Investigation, Validation, Data curation.

Yang Liu: Investigation, Software, Formal analysis.

Jinghua Chen: Investigation, Resources.

Yinshui He: Conceptualization, Supervision, Funding acquisition, Writing – review and editing.

References

[1] D. Deng, H. Murakawa, W. Liang, “Numerical simulation of welding distortion in large structures,” *COMPUT METHOD APPL M,* vol. 196, no. 45, pp. 4613-4627, 2007.

[2] C. H. Zhang, J.-h. Feng, X. Wang, “Research on the Seismic Design of High-rise Steel Building Based on Security Perspective,” *INT J SMART HOME,* vol. 10, pp. 253-262, 2016.

[3] X. L. Wang, Y. R. Nan, Z. J. Xie, Y. T. Tsai, J. R. Yang, C. J. Shang, “Influence of welding pass on microstructure and toughness in the reheated zone of multi-pass weld metal of 550 MPa offshore engineering

steel," *MAT SCI ENG A-STRUCT,* vol. 702, pp. 196-205, 2017.
[4] C. H. Zhang, S. Li, J. M. Sun, Y. F. Wang, D. A. Deng, "Controlling angular distortion in high strength low alloy steel thick-plate T-joints," *J MATER PROCESS TECH,* vol. 267, pp. 257-267, 2019.
[5] Z. Chen, Z. C. Chen, R. A. Shenoi, "Influence of welding sequence on welding deformation and residual stress of a stiffened plate structure," *OCEAN ENG,* vol. 106, pp. 271-280, 2015.
[6] S. Cai, Y. Zhang, J. Wu, F. Wu, "A fuzzy finite element model based on the eigenstrain method to evaluate the welding distortion of T-joint fillet welded structures," *J MANUF PROCESS,* vol. 77, pp. 451-462, 2022.
[7] J. Shin, J. Kim, "Numerical and Experimental Study on Welded and Bolted Steel Beam-Column Connections Subjected to Cyclic Loading," *J EARTHQ TSUNAMI,* vol. 11, no. 4, pp. 1750014, 2017.
[8] S. Liu, Z. Wu, W. Zhou, H. Zhou, K. Zhang, D. Yin, Y. Lei, Y. Qiu, "A review of welding simulation methods for large components," *PROG NAT SCI-MATER,* vol. 33, no. 5, pp. 551-568, 2023.
[9] E. Dogan, M. Ay, M. Kurtulmus, A. I. Yukler, A. Etyemez, "Effects of welding parameters on the angular distortion of welded steel plates," *OPEN CHEM,* vol. 20, no. 1, pp. 417-423, 2022.
[10] P. K. Taraphdar, R. Kumar, A. Giri, C. Pandey, M. M. Mahapatra, K. Sridhar, "Residual stress distribution in thick double-V butt welds with varying groove configuration, restraints and mechanical tensioning," *J MANUF PROCESS,* vol. 68, pp. 1405-1417, 2021.
[11] C. Zhang, S. Li, J. Sun, Y. Wang, D. Deng, "Controlling angular distortion in high strength low alloy steel thick-plate T-joints," *J MATER PROCESS TECH,* vol. 267, pp. 257-267, 2019.
[12] M. Ghafouri, A. Ahola, J. Ahn, T. Björk, "Welding-induced stresses and distortion in high-strength steel T-joints: Numerical and experimental study," *J CONSTR STEEL RES,* vol. 189, pp. 107088, 2022.
[13] G. Fu, M. I. Lourenço, M. Duan, S. F. Estefen, "Influence of the welding sequence on residual stress and distortion of fillet welded structures," *MAR STRUCT,* vol. 46, pp. 30-55, 2016.
[14] H. T. Ding, W. Y. Zhang, Z. Y. Zhang, D. D. Yin, W. T. He, D. Xie, "Influence of welding sequences and boundary conditions on residual stress and residual deformation in DH36 steel T-joint fillet welds," *THIN WALL STRUCT,* vol. 204, 2024.
[15] S. Geng, Y. Li, P. Jiang, Y. Wang, J. Jin, C. Han, "Influence of welding sequences on residual stress and deformation of U-rib components fabricated by laser-arc hybrid welding," *J MATER RES TECHNOL,* vol. 35, pp. 726-742, 2025.
[16] X.F. Zhao, H. Panzer, A. Zapata, F. Riegger, S. Baehr, M. F. Zaeh, "Deposition sequence optimization for minimizing substrate plate distortion using the simplified WAAM simulation," *J MANUF SYST*, vol. 81, pp. 103-116, 2025.
[17] J. Yi, Z. Chen, C. Sun, J. Li, D. Li, "Prediction of welding deformation in stiffened structures using a data-driven Def-GAN model," *J CONSTR STEEL RES,* vol. 221, pp. 108916, 2024.
[18] S. P. Cai, Y. K. Zhang, J. X. Wu, F. M. Wu, "A fuzzy finite element model based on the eigenstrain method to evaluate the welding distortion of T-joint fillet welded structures," *J MANUF PROCESS,* vol. 77, pp. 451-462, 2022.
[19] M. Karimi, N. Mokhtari, J. Jelovica, "Deep learning for predicting welding distortions in T-joints," *WELD WORLD*, 2025.
[20] A. Hammad, C. Churiaque, J. M. Sánchez-Amaya, Y. Abdel-Nasser, "Experimental and numerical investigation of hybrid laser arc welding process and the influence of welding sequence on the manufacture of stiffened flat panels," *J MANUF PROCESS,* vol. 61, pp. 527-538, 2021.
[21] B. Q. Chen, C. G. Soares, "Effect of welding sequence on temperature distribution, distortions, and residual stress on stiffened plates," *INT J ADV MANUF TECH,* vol. 86, no. 9-12, pp. 3145-3156, 2016.
[22] A. Khoshroyan, A. R. Darvazi, "Effects of welding parameters and welding sequence on residual stress and

distortion in Al6061-T6 aluminum alloy for T-shaped welded joint," *T NONFERR METAL SOC,* vol. 30, no. 1, pp. 76-89, 2020.

[23] T. Bajpai, A. K. Nyati, P. Sharma, P. K. Gupta, "Numerical and Experimental Investigation on Effects of Welding Sequence on Distortions in Fillet-Welded AA6061-T6 Joints," *J MATER ENG PERFORM,* vol. 33, no. 20, pp. 10980-10994, 2024.

[24] Y. L. Zhang, L. Tian, "The effect of joint configuration on residual stress and distortion of the 304 stainless steel multi-pass welded joints," *MATER TODAY COMMUN,* vol. 30, 2022.

[25] X. Gui, Y. Zhang, D. You, X. Gao, "Numerical simulation and test for influence of laser arc hybrid welding sequence on 304 stainless steel T-joint," *TRANS CHINA WELD INST,* vol. 42, no. 12, pp. 34-39, 2021.

[26] M. Kim, M. Kang, H. Chung, "Simplified welding distortion analysis for fillet welding using composite shell elements," *INT J NAV ARCH OCEAN,* vol. 7, no. 3, pp. 452-465, 2015.

[27] Q. Shao, T. Xu, T. Yoshino, N. Song, "Multi-objective optimization of gas metal arc welding parameters and sequences for low-carbon steel (Q345D) T-joints," *J IRON STEEL RES INT,* vol. 24, no. 5, pp. 544-555, 2017.

[28] Y. Rong, Y. Chang, J. Xu, Y. Huang, T. Lei, C. Wang, "Numerical analysis of welding deformation and residual stress in marine propeller nozzle with hybrid laser-arc girth welds," *INT J PRES VES PIP,* vol. 158, pp. 51-58, 2017.

[29] M. Ghafouri, A. Ahola, J. Ahn, T. Björk, "Numerical and experimental investigations on the welding residual stresses and distortions of the short fillet welds in high strength steel plates," *ENG STRUCT,* vol. 260, 2022.

[30] C. Zhang, S. Li, L. Hu, D. Deng, "Effects of pass arrangement on angular distortion, residual stresses and lamellar tearing tendency in thick-plate T-joints of low alloy steel," *J MATER PROCESS TECH,* vol. 274, pp. 116293, 2019.

[31] L. Lan, G. Shao, Y. Zhang, Y. Wang, "Influence of Welding Sequence on Residual Stress and Deformation of T-Joint of Q690 Steel," *J NORTHEAST UNIV NAT SCI,* vol. 41, no. 12, pp. 1741-1746, 2020.

[32] Y. H. P. Manurung, R. N. Lidam, M. R. Rahim, M. Y. Zakaria, M. R. Redza, M. S. Sulaiman, G. Tham, S. K. Abas, "Welding distortion analysis of multipass joint combination with different sequences using 3D FEM and experiment," *INT J PRES VES PIP,* vol. 111, pp. 89-98, 2013.

[33] C. Li, H. Zhai, L. W. Zhu, Z. H. Liu, J. G. Ma, X. F. Zhu, Q. Liu, "Numerical investigation of welding deformation diminution for double shell structure using the layered inherent strain," *NUCL ENG TECHNOL,* vol. 57, no. 2, 2025.

[34] V. Sharma, A. S. Shahi, "Effect of groove design on mechanical and metallurgical properties of quenched and tempered low alloy abrasion resistant steel welded joints," *MATER DESIGN,* vol. 53, pp. 727-736, 2014.

[35] Q. He, G. R. Li, Y. Guo, H. G. Zhou, L. Li, "Effect of Bevel Type and Plate Thickness on Temperature Field and Deformation of Reinforced Slabs," *J MATER ENG PERFORM,* vol. 33, no. 20, pp. 10895-10909, 2024.

[36] W. C. Yi, J. WenGuang, "Influence of welding groove on residual stress and distortion in T-joint weld," *IOP CONF SER: MATER SCI ENG,* vol. 733, pp. 012010-012010, 2020.

[37] Y. F. Wang, G. J. Feng, X. W. Pu, D. Deng, "Influence of welding sequence on residual stress distribution and deformation in Q345 steel H-section butt-welded joint," *J MATER RES TECHNOL,* vol. 13, pp. 144-153, 2021.

[38] J. Goldak, A. Chakravarti, M. Bibby, "A NEW FINITE-ELEMENT MODEL FOR WELDING HEAT-SOURCES," *METALL MATER TRANS B,* vol. 15, no. 2, pp. 299-305, 1984.